JOURNAL OF PROPULSION AND POWER
Vol. 25, No. 6, November–December 2009

Acoustics, Vortex Shedding, and Low-Frequency Dynamics Interaction in an Unstable Hybrid Rocket

C. Carmicino*
University of Naples "Federico II," 80125 Naples, Italy

DOI: 10.2514/1.42869

This paper deals with an experimental investigation into the stability behavior of a hybrid rocket where gaseous oxygen is fed with either an axial conical subsonic nozzle or a radial injector. The influence of the oxidizer-injection configurations on the motor stability is thoroughly examined. These distinct oxidizer-injection techniques allowed unveiling key and so far unreported features of the hybrid rocket combustion stability, especially emphasizing the role of vortex shedding which occurs in both the pre- and postcombustion chamber. Axial and radial injectors caused completely stable and unstable combustor operations, respectively, and this fact has been attributed to the fluid dynamics and unsteady heat release at the entrance of the fuel grain port. In particular, the unstable combustion in the radial-flow injector motor was dominated by low-frequency pressure oscillations, around 10–20 Hz. These low-frequency pressure oscillations were always accompanied by longitudinal acoustic modes. In some cases, the pressure oscillations abruptly increased, reaching peak-to-peak amplitude close to 70% of the mean chamber pressure, which is somewhat unusual for hybrid engines. Vortex shedding in the aft-mixing chamber is considered as the main driving mechanism of this latter behavior.

Nomenclature

c	=	average speed of sound in the combustion chamber, $\sqrt{\gamma(RT)_{\text{av}}}$
c^*	=	characteristic exhaust velocity
D	=	fuel port diameter
$\bar{D}$	=	time–space-averaged fuel port diameter
D_t	=	exhaust nozzle throat diameter
f	=	frequency
$\bar{G}_{\text{ox}}$	=	time–space-averaged oxidizer mass flux
L	=	combustion chamber length
L_f	=	fuel grain length
l	=	exhaust nozzle length
$\dot{m}$	=	mass flow rate
O/F	=	oxidizer to fuel mixture ratio
p	=	combustion chamber pressure
R	=	gas constant
$\bar{\dot{r}}$	=	time–space-averaged regression rate
Sr	=	Strouhal number
s	=	fuel grain thickness
T	=	gas temperature
U	=	average gas velocity
$\mathcal{V}$	=	combustion port volume
γ	=	specific heat ratio
η	=	combustion efficiency
τ	=	ultrasound time of flight
Ψ	=	function of specific heat ratio

Subscripts

H	=	Helmholtz mode
hy	=	intrinsic hybrid instability
j	=	gas jet
ox	=	oxidizer
s	=	sampling
th	=	theoretical
VS-aft	=	vortex shedding in the postchamber
VS-pre	=	vortex shedding in the prechamber
$1L$	=	first longitudinal acoustic mode

Received 21 December 2008; revision received 28 July 2009; accepted for publication 8 August 2009.

*Consultant, Department of Aerospace Engineering, Piazzale Tecchio 80; currently General Electric Oil and Gas, Via F. Matteucci 2, 50127 Firenze, Italy. AIAA Member.

I. Introduction

PROPULSION systems such as solid and liquid propellant rockets and airbreathing engines, like ramjets, are known to have a tendency toward unstable operation, that is, toward what is commonly referred to as combustion instability [1,2]. From a general point of view, strong instabilities in combustors have to be avoided because they can cause excessive mechanical vibrations on the engine and the vehicle structure, which can damage delicate payloads and control systems, or even lead to structural failure. Mild instabilities, on the other hand, may even improve combustion efficiency by promoting fuel–oxidizer mixing as, for example, in pulse combustors [3] and hybrid rockets [4]. The latter, like the aforementioned propulsion systems, suffer from combustion instability. In fact, the open literature [5,6] reports that hybrid rockets typically show finite amplitude, up to 20% rms of the mean, low-frequency chamber pressure oscillations. These pressure oscillations have a predominant frequency in the range of tens of hertz, and they often take place together with acoustic frequency oscillations. Here, as acoustic oscillations are intended, the chamber pressure oscillations having a frequency close to that of the chamber longitudinal acoustic modes.

The low-frequency instability is intrinsic of hybrid engines; it has been described by means of a linear model [7,8] that combines the thermal lag in the solid grain, the gas-phase combustion, and the gas dynamics in the combustion chamber, yielding a universal scaling formula for the primary hybrid oscillation frequency

$$f_{\text{hy}} = \frac{0.48}{\tau_{\text{bl}}} = 0.234\left(2 + \frac{1}{O/F}\right)\frac{4}{\pi}\frac{\dot{m}_{\text{ox}}(RT)_{\text{av}}}{L_f p D^2} \tag{1}$$

where τ_{bl} is the so-called boundary-layer delay time [7], that is, the characteristic response time to disturbances in the boundary layer over the grain surface.

However, although this theoretical model can predict the pressure oscillation dominant frequency, it is unable to explain if and when these low-frequency instabilities will develop in the combustor. Actually, there are hybrid motors where pressure-time trace is very

smooth and motors, with the same propellants, size, and operating parameters where that is not so [9]. In particular, changing the oxidizer-injection configuration from axial to radial flow has been demonstrated to generate instabilities [5,10]. In that case, the occurrence of pressure oscillations has been attributed to a flame-holding inefficiency (typical of solid-fuel ramjets) ensuing from the different fluid-dynamic conditions at the head end of the grain when switching from the former to the latter injection configuration. In general, it has been found that any injector design producing a strong recirculation zone gave rise to a stable combustion. Boardman et al. [5] conducted a systematic research into the influence of the gaseous oxidizer injector on the motor stability. By varying the head-end motor configuration with different injectors, radial, axial and hollow cone, and the fore grain surface (combustion inhibited or not) they observed two primary oscillation frequencies when the radial injector was used: a low-frequency, nonacoustic mode in the range of 8–20 Hz, and the combustion chamber first longitudinal acoustic mode. They concluded that, due to the inherently unstable diffusion-controlled hybrid combustion, when efficient flame holding was not accomplished by means of proper gas recirculation, the first acoustic mode, activated by the grain leading-edge diffusion flame oscillations, drove the increase in the fuel regression rate which, in turn, resulted in increased chamber pressure. However, their deduction can be questionable [11] and it was not supported by any data on the instantaneous regression rate.

The main feature emerging from what is cited herein is that hybrid engines generally exhibit low-frequency instability, which seems preferably excited when no sufficient propellant mixing is promoted at the entrance of the fuel grain. In the context of the current investigation, this condition is achieved by means of a radial injector, whereas an axial injector is employed to generate larger recirculation and mixing [9].

Interaction between vortex shedding and chamber acoustics is a well-known cause for significant increase in acoustic pressure amplitude, which can lead to combustion instability in solid rocket motors [12–14]. This phenomenon can be observed especially when slotted grains are employed [15] or, in general, if a sudden change of cross-sectional area of the combustion chamber exists. Nevertheless, no adequate attention has been paid to vortex shedding in hybrid rockets, as also noted in [16]. In these motors, precombustion and aft-mixing chambers are usually mated to the fuel grain ends; in this arrangement, large-scale vortex structures can develop, detach, and impinge on a solid surface at a suitable distance downstream of the shear layer origin, that being a potentially important mechanism for the onset of large pressure oscillations.

This paper highlights the central role of vortex shedding, at least in the amplification of instability, with the presentation of the static engine firing results obtained from a laboratory-scale hybrid rocket where gaseous oxygen was supplied into cylindrical, polyethylene, or hydroxil-terminated polybutadiene (HTPB) fuel grains. The motor stability is analyzed by comparing the influence of an axial subsonic nozzle and a radial injector on the fluctuations of chamber pressure and instantaneous fuel-regression rate. Real-time regression rate was measured with the ultrasound pulse-echo technique. As far as the author knows, applications of this technique in unsteady conditions have been directed to solid propellant motors [17,18], but this is the first time ultrasounds are used for frequency response analyses in a hybrid rocket. However, it has to be specified that no corrections from the unsteady thermal effect on the ultrasound measurements have been made, so that regression rate results have to be considered as preliminary.

Most of the firing tests were conducted on the radial-injection motor because the axial injector has been the subject of past research [9,19]. Tests will be shown where pressure oscillations amplitude reaches the remarkable value of 65%, peak to peak, of the mean chamber pressure. This behavior, verified with the radial injector in certain conditions, was not encountered with the axial injector, whatever were the port diameter and the chamber pressure, in the ranges of 16–75 mm and 10–20 atm, respectively. Vortex shedding in the aft-mixing chamber will be demonstrated to be responsible for this issue.

II. Experimental Setup and Motor Configuration

In this section, the lab motor and the test apparatus are described. For an exhaustive account on this subject, also refer to the papers of [9,19].

A. General Layout

A scheme of the test facility is shown in Fig. 1. Gaseous oxygen is supplied by a reservoir of 8 cylinders; in this experimental campaign, oxygen flow rates were in the range of 0.055–0.16 kg/s.

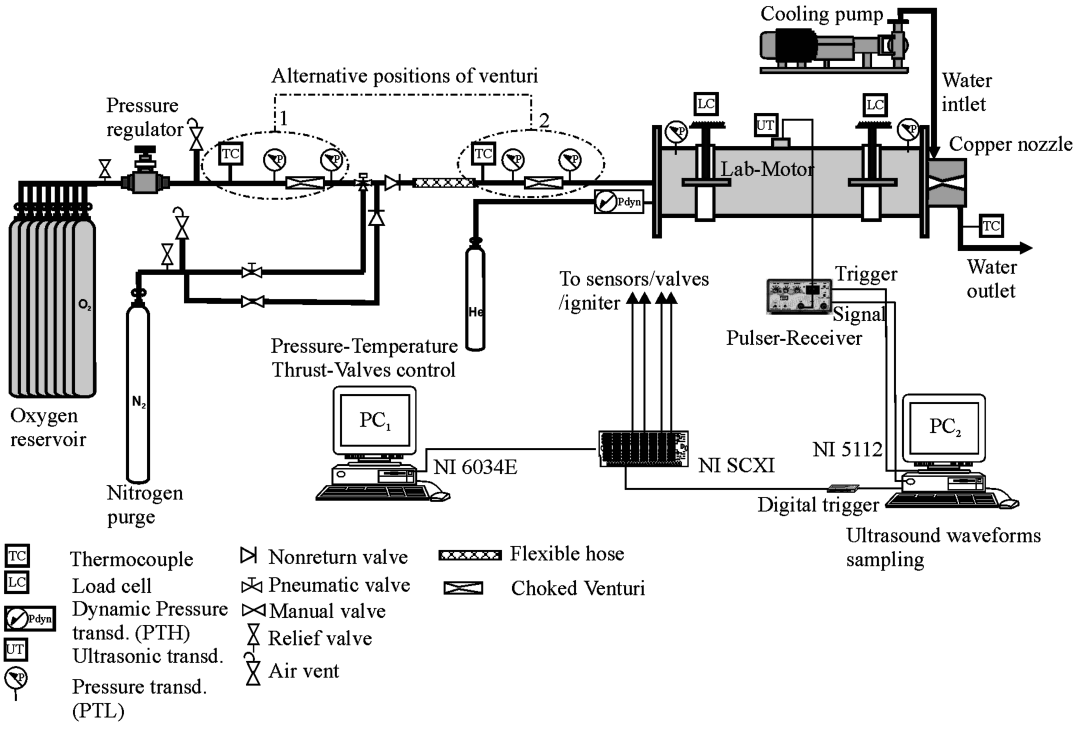

Fig. 1 Test facility.

The oxygen mass flow rate is evaluated by measuring the gas temperature (with a copper-constantan thermocouple) and pressure at a section upstream of the throat of a home-designed choked venturi tube. Installing this device was mandatory for decoupling the combustion chamber dynamics from the one of the rocket feed system. Furthermore, to minimize the capacitance of the gas delivery line, after a number of tests, the venturi was moved from the initial position on the line to a position much closer to the injector (labeled with 1 and 2 in Fig. 1, respectively), reducing the volume of the line downstream of the venturi throat by about 90%. Thus, constant oxidizer mass flow was considered, independently of pressure oscillations in the motor. The effectiveness of this system will be discussed later.

High-density polyethylene (HDPE) and HTPB fuel grains with one circular port and slightly different lengths (on the order of 580 and 535 mm, depending on the particular injector assembly) were tested. Several initial inner diameters (16, 25, 50, and 75 mm) were chosen to explore a wide range of mass fluxes, and purely geometrical and fluid-dynamic effects.

Upstream and downstream of the fuel grain, a dump plenum and an aft-mixing chamber were set up, respectively. A water-cooled converging-diverging nozzle with 16 mm throat diameter, 82 mm length, and 2.44 area ratio, made of copper alloy, ensures long duration firings with no throat erosion.

Low-frequency chamber pressure was measured by two capacitive transducers (which will be referred to as PTL for further reference), Setra model 280E, set up in the prechamber and in the aft-mixing chamber. High-frequency pressure oscillations were obtained in the dump plenum using a PCB helium-bleed dynamic pressure gauge model 123A (which will be referred to as PTH), flush mounted on the motor forward closure (see Figs. 1 and 2).

The motor is suspended from the test bench by four load cells, which allows computing of the thrust as the sum of the loads measured by each cell. Motor ignition was accomplished by means of a pyrotechnic cartridge electrically primed.

The analog signals coming from thermocouples, pressure transducers, and load cells were sampled at 10 kHz, digitally converted, processed, and recorded on the hard disk by a National Instruments (NI) SCXI system interconnected with PC_1 in Fig. 1 via a NI 6034 E PCI board with 16 bit resolution. No antialiasing analog filters were used. With this equipment and using a dedicated software developed in LabView 7, the motor is ignited and the firing test is completely automated. All the signals were saved in a binary format for post-processing and in text format, after averaging down the data to 100 Hz ("boxcar averaging").

The instantaneous regression rate was measured by means of the ultrasound pulse-echo technique. One ultrasonic transducer, placed around the middle of the chamber (Fig. 1), was employed to acquire the local grain thickness variation over time. The ultrasonic transducer is a Panametrics Videoscan V114-SB of $\frac{3}{4}$ in nominal diameter and 1 MHz central frequency. The waves emitted by the transducer are electrically generated and then received and amplified by a pulser/receiver unit (Panametrics model 5072PR) with 1 kHz pulse repetition frequency (PRF). A cross-correlation-based technique was applied to process the ultrasound waveforms, as discussed in a forthcoming section.

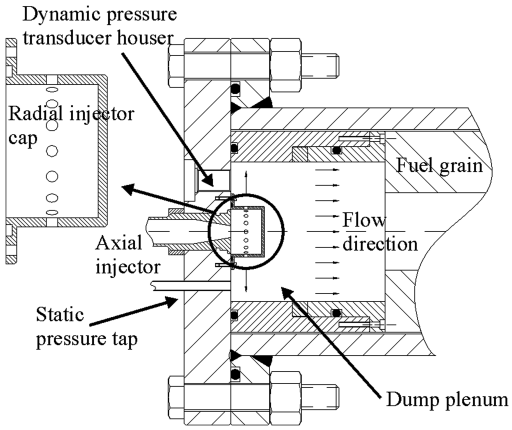

Fig. 2 Axial injector/radial injector and dump plenum at the head end of the motor.

B. Oxygen Injectors

Axial- and radial-injector configurations were employed to generate completely different conditions for the oxidizer at the entrance of the fuel port. With the former, oxygen is axially injected into the combustion chamber through a converging nozzle whose exit diameter is 8 mm. The exit Mach number was at most 0.35. The radial-injection system is made by a radial-injector cap, shown in Fig. 2, which, when assembled on the injection flange, produces a radial flow in a dump plenum (in stainless steel and slightly longer than the prechamber used with the axial-injector setup), via 16 equally spaced 2.5-mm-diam orifices around the periphery of the cap. The radial injector equivalent exit area is thus 56% larger than the axial injector one. This design has been aimed at trying to maintain almost the same gas velocity through both injectors. The reason why this implies a larger area of the radial injector will be clear in the following.

The main features of the flowfield in the motor forward end ensuing from the two injector arrangements can be deduced from the steady-state streamlines reported in Fig. 3 (here, the fuel grain has 50 mm port diameter, the oxygen mass flow rate is 0.1 kg/s, and the pressure at the exit plane is 12 atm).

The commercial code Fluent 6.2 was used to solve the nonreactive flowfield in the motor for different port diameters [20]. The exhaust nozzle was not included in the computational domain. The gas was oxygen at room temperature, the mass flow rate at the inlet and the aft chamber exit pressure were set equal to those experimentally measured. No blowing from the side wall was considered, the flow characteristics at the motor head end being the main subject of investigation. The flow was supposed compressible and turbulent; the "k-ε realizable" turbulence model was employed. For the axial injector, an axially symmetric flowfield was solved, whereas, for the radial-injector motor, the flowfield was studied in one-sixteenth of the cylindrical geometry (corresponding to the slice containing one hole of the injector cap), assigning rotational periodicity on the axial planes. The basic results are briefly summarized here. First, the pattern of the streamlines inside the radial-injector cap (Fig. 3b) indicates that the gas accelerates through the peripheral holes due to the gas turning, which produces a contraction of the hole effective exit section and, accordingly, a velocity increase. This effect has been reduced by enlarging the radial-injector equivalent area with respect to the axial injector, as previously mentioned.

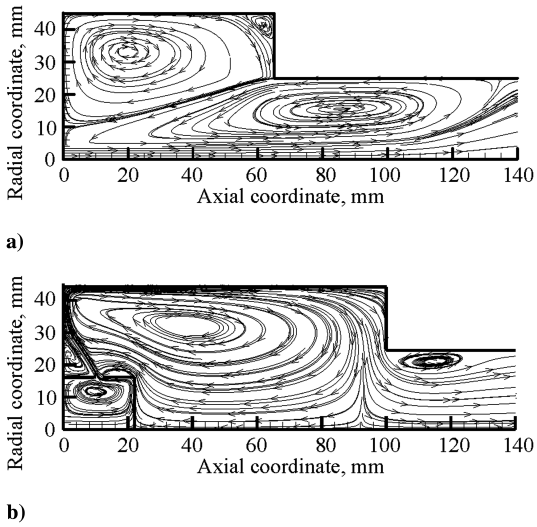

Fig. 3 Streamlines at the head end of the motor: a) axial injector, b) radial injector ($D_0 = 50$ mm).

With the axial injector, a main counterclockwise-rotating vortex is established in the inlet region of the grain (Fig. 3a). This broad vortex is bounded, on the front side, by the zone of oxygen impingement on the grain surface, which moves more downstream along the grain with larger port diameters. In the precombustion chamber, another large vortex, clockwise rotating, is formed delimiting the main one on the backside. The oxygen jet impingement on the surface entails a nonuniform convective heat transfer distribution such that the wall heat flux and thus the regression rate rise from the grain inlet, attaining a maximum in the jet impingement region and, farther downstream, gradually decrease along the combustor axis. As was shown in an earlier paper [19], this configuration results in increased regression rates (up to 3 times larger, for very low-mass fluxes), lower dependence of regression rate itself on mass flux (smaller mass flux exponent, $n = 0.37$), and sensibly higher combustion efficiency, about 98%, depending on the recirculation zone extent [9].

With the radial injector, the recirculation zone in the port entry is much narrower than with the axial injector, and it has a substantially different nature. Indeed, vorticity is generated due to the fluid vena contracta at the sudden reduction of the chamber cross section; the flow turning, then, produces a separated region, which may be likely a source of periodic shedding of vortices. A large clockwise-rotating vortex, which reduces the velocity at the inlet of the grain, is formed in the dump plenum. In this case as well, when the port diameter is increased, the reattaching distance moves downstream along the grain. However, this configuration generates lower and more uniform (along the grain axis) regression rates and a higher dependence on the mass flux (mass flux power exponent $n = 0.77$) in comparison to the axial injection [21].

III. Experimental Data Processing Techniques

A. Ultrasound Signals Analysis

The ultrasound waveforms, emitted and acquired with a PRF equal to 1 kHz, were sampled with 10 MHz rate by a NI 5112 PCI digitizer having 32 MB onboard memory and 8 bit resolution, and recorded by PC_2, while PC_1 was deputed to the acquisition of other experimental data and to the test control (see Fig. 1). A digital trigger was used for synchronizing the two separate acquisitions. With this sampling frequency, the fuel thickness is determined with an accuracy of about 0.11 mm for HDPE and 0.075 mm for HTPB whose speeds of sound, at reference conditions, are around 2300 and 1500 m/s, respectively. This accuracy is actually increased, because an interpolation method was used.

The signals were analyzed by a cross-correlation technique to compute the time delay from the echo corresponding to the interface between the coupling insert and the outer surface of the grain to the backwall echo related to the grain inside surface (Fig. 4).

This measurement mode does not require one to compensate the measure for the increment caused by the transit time through the transducer wear plate and the coupling fluid, nor for the cable delay, or any other offset due to rise time or frequency content of the detected echo. With the cross-correlation method, the time of flight through the propellant is estimated by searching for the maximum of the coefficient of correlation between the first and second interface

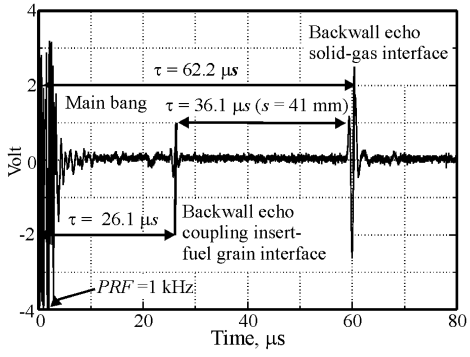

Fig. 4 Ultrasound waveform and relevant echoes (HDPE).

echoes in Fig. 4. Because the true location of the correlation function maximum is, of course, not constrained to discrete increments, but it may fall between the discrete sampling points, a parabolic fit was used to improve the estimation accuracy of the time of flight and then of the fuel instantaneous thickness [22]. Note that, with PRF= 1 kHz, an interpolation method is necessary for the regression rate calculation because, even with regression rates on the order of 1 mm/s, the time-of-flight variation over a time step $\Delta t = \mathrm{PRF}^{-1}$ is on the order of 10^{-3} μs, which is 100 times less than the basic accuracy of the thickness measurement. This technique is less prone to bias compared to the methods, often used, which rely on the determination of some signal zero crossing [23]. In fact, for media that exhibit frequency-dependent attenuation like propellants and dispersion (that is, the frequency dependence of phase velocity), the pulse shape may change with thickness, thereby altering the zero-crossing locations and affecting the time-of-flight estimates [24].

The grain thickness s was calculated from the waves' propagation time, assuming the wave speed in the fuel to be constant [25,26], namely,

$$s = s_0 \frac{\tau}{\tau_0} \tag{2}$$

where τ_0 and s_0 are the prefiring transit time and fuel thickness, respectively. The thickness data were low-pass filtered (30 Hz cutoff frequency), then a numerical central formula was applied to take the thickness derivative for the regression rate calculation.

B. Spectral Analysis of Pressure and Regression Rate

Sampled data were processed with two slightly different procedures depending on the operation to be performed, that is, a global spectral analysis or a joint time-frequency analysis.

Pressure data output by the PTH transducer were symmetrically zero padded to the next power of 2 and windowed through a Hanning window with the purpose of minimizing the spectral leakage, for the calculation of the overall (i.e., over the entire firing) spectra. Discontinuities between the original pressure signal and the added zeroes were eliminated by subtracting from each sample the pressure offset. Then, fast Fourier transform (FFT) was performed to display the overall spectrum. Regression rate data were treated in the same way. Additionally, to remove the power line interference at 50 Hz and its higher harmonics from the PTH signals, the points of the amplitude spectrum at the line interference harmonics were substituted with an average of the nearby points in the spectrum, hence the inverse FFT was computed to give back the filtered signal in the time domain.

Regression rate and pressure data acquired by PTH (the latter once filtered from the spurious power line harmonics) were both bandpass filtered in the range 1–60 Hz and high-pass filtered above the latter cutoff frequency, with the twofold aim of, respectively, eliminating the dc signal and taking apart the slower varying (low-frequency) components from the higher-frequency ones. This, in particular, would allow one to separate nonacoustic from acoustic pressure fluctuations. Phase shift resulting from all the filtering processes was eliminated as follows: the signal was first filtered with increasing time and then filtered back from the last point with decreasing time [27].

The resulting data were analyzed with the short-time-Fourier-transform technique to map the oscillation amplitude over the joint frequency-time domain. The short-time Fourier transform (STFT) of the generic signal $x(t)$ is defined by the following relationship [28]:

$$\mathrm{STFT}\,(t_0, f) = \int_{-\infty}^{+\infty} x(t) w(t - t_0) e^{-j2\pi f t}\,\mathrm{d}t \tag{3}$$

in which the function $w(t)$ is commonly referred to as the analysis window and j is the imaginary unit. STFT is, then, a function of the frequency f and of the time instant t_0 in which the window function is centered, and represents the Fourier transform of the given signal around t_0. As a consequence, it provides information about when and at what frequency a given signal event occurs.

Both the low- and high-frequency components, derived through the filtering operation just described, were transformed to yield the so-called spectrogram (i.e., the squared magnitude of STFT); the following discrete Gaussian window was used

$$w(k) = \alpha \exp\left[-\frac{1}{2}\left(2.5\frac{k-f_s}{f_s}\right)^2\right], \qquad 0 \le k \le 2f_s \qquad (4)$$

where α is a normalizing factor and f_s is the signal sampling rate. In Eq. (4) the window period was set to 2 s (that is, the window length was $2f_s$ points); the time increment was 1 s, resulting in 50% overlapped data.

IV. Results and Discussion

This section will proceed following the logical path which has led to the formulation of the conclusions drawn later; this starts with the observation of pressure-time traces.

The test table, containing the motor operating conditions and some average parameters derived from them, is reported in Table 1. The label appearing in the first column will identify every test. The time–space-averaged regression rate was simply calculated from the fuel mass loss, and the average oxidizer mass flux was defined based on the average port diameter, which was calculated from the final grain mass [19].

Note that the fuel grains used with the radial injector are generally shorter because the prechamber is longer in this configuration (see Fig. 3). Slightly different lengths (at most 2%) are only due to particular manufacturing requirements. When short grains (L_f= 532 mm) were used with the axial injector, this was due only to their immediate availability. Grain length changes were accommodated with several thermal insulations having proper thickness.

A. Time Domain and Overall Spectra

A striking feature immediately appearing from a comparison between chamber pressure in the radial- and axial-injection motors is that, with the same propellants, initial fuel port diameter, and average chamber pressure, the radial injection produces very high-amplitude pressure fluctuations. This is shown in Figs. 5–7, where down-sampled chamber pressure obtained with the slow-response transducer (PTL) in the prechamber is plotted versus time for six tests performed in similar conditions, three with the radial injector and three with the axial injector. The first two tests (test 11-R and test 4-A) used HTPB fuel, whereas the others used HDPE. Whereas Fig. 5 displays the entire motor ignition, operation, and shutdown sequence,

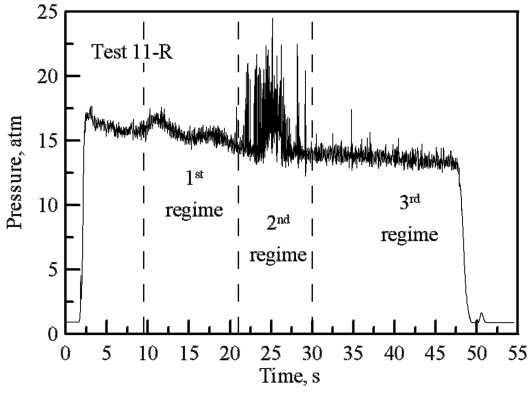

a)

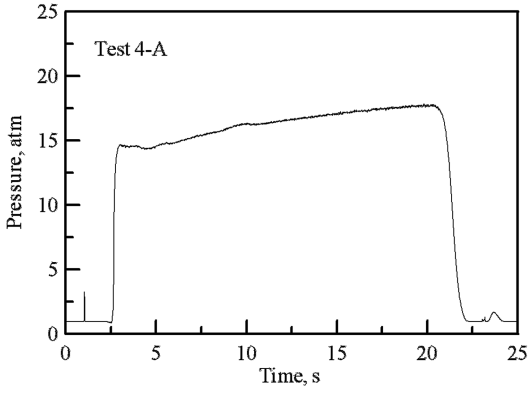

b)

Fig. 5 Chamber pressure versus time: a) radial injector, b) axial injector.

Figs. 6 and 7 represent only the operation phase with the aim of emphasizing the pressure oscillations amplitude characteristics.

According to Fig. 5a, relating to a test with 25 mm port initial diameter, three distinct regimes of operation can be observed during the firing. Within the first of these, over the time period between 10–20 s, chamber pressure slightly shifts upward and falls 2 times (around 10–13 s and 15–20 s). At the same time, the mean regression

Table 1 Tests matrix

Test	Fuel	D_0, mm	L_f, mm	$\dot{m}_{ox}$, kg/s	p, atm	$\bar{G}_{ox}$, kg/m^{2}s	O/F	$\bar{\dot{r}}$, mm/s	$\bar{D}$, mm	f^c, Hz
1-R[a]	HDPE	25	533	0.149	13.3	78.0	5.03	0.376	49.2	13.7
2-R	HDPE	25	532	0.145	13.5	103.1	4.82	0.445	59.6	13.7
3-R	HDPE	75	532	0.141	11.2	28.9	6.26	0.178	78.8	6.9
4-R	HDPE	52	532	0.145	12.9	54.4	5.07	0.306	58.2	12.5
5-R	HTPB	50	538	0.161	15.3	52.1	3.75	0.436	62.8	9.5
6-R	HTPB	50	535	0.157	16.5	47.1	3.09	0.492	65.1	9.9
7-R	HTPB	50	542	0.152	14.0	44.6	3.62	0.403	65.9	15.7
8-R	HTPB	25	542	0.139	14.2	57.4	3.16	0.500	55.4	13.8
9-R	HTPB	50	545	0.160	16.2	45.6	3.57	0.422	66.8	13.6
10-R	HTPB	25	538	0.055	6.7	29.4	1.74	0.411	48.8	9.0
11-R	HTPB	25	545	0.141	14.7	65.6	2.86	0.589	52.4	15.2
12-R	HDPE	16	532	0.154	16.4	119.1	3.82	0.626	40.6	12.0
13-R	HDPE	40	533	0.142	13.0	59.0	5.08	0.319	55.4	17.7
14-R	HDPE	70	533	0.138	11.7	31.1	5.45	0.212	75.2	11.5
15-R	HDPE	40	533	0.158	14.4	63.2	5.33	0.333	56.4	15.0
16-R	HDPE	50	533	0.118	11.7	44.9	4.92	0.260	57.8	6.0
1-A[b]	HDPE	25	578	0.110	13.8	64.6	2.66	0.535	37.9	——
2-A	HDPE	50	532	0.094	11.6	30.0	2.72	0.409	63.4	——
3-A	HDPE	75	532	0.092	12.1	17.0	1.99	0.346	82.1	——
4-A	HTPB	25	574	0.133	16.2	94.0	1.94	0.931	42.4	——

[a]R refers to tests with the radial injector.
[b]A refers to tests with the axial injector.
[c]Dominant frequency measured over the test.

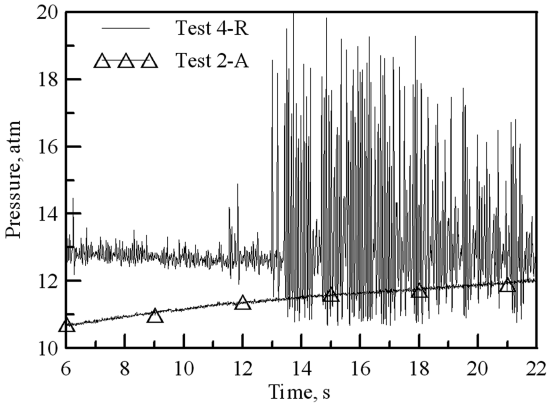

Fig. 6 Chamber pressure versus time, radial injector and axial injector.

rate also shifts upward, as will be discussed in detail later in the paper. This phenomenon has been commonly referred to as "dc shift" and has been studied extensively in the field of solid rocket combustion instability [29]. An attempt to explain the mechanism leading to the dc shift in hybrids has been made by considering the nonlinear characteristics of the thermal lag model previously mentioned [30]. However, the conclusion has been that the regression rate shift cannot be caused by these nonlinear effects.

During this phase, the oscillation peak-to-peak amplitude is around 11% of the pressure baseline value. After that, a second regime can be identified between 21–30 s, in which pressure oscillations arise with much larger amplitude (45–50% of the mean pressure peak to peak). A similar behavior is noted in Fig. 6; starting from about 13 s, pressure fluctuations in the radial-injector motor are even more severe, reaching a peak-to-peak amplitude of 65% of average pressure (here, the fuel grain has 52 mm initial diameter). Also, in this case, dc shift is present. Finally, in the third regime, mean pressure continuously decreases (no dc shift is detectable), maintaining the same level of oscillation as in the early stage of firing and the first regime.

These tests are somewhat unique, because the literature on hybrid rockets, unlike solid propellant motors, seldom reports similar cases [11]. Sharp pressure spikes, actually, were observed in large motors [31] and their occurrence was attributed to inadequate vaporization of liquid oxygen and flame holding at the leading edge of the boundary layer developing on the grain surface. However, Fig. 7 shows a case resembling those found in most of the literature: here, the fuel port diameter is 75 mm, and the chamber pressure in the radial-injector motor oscillates with almost the same amplitude (around 17%) all over the test. As opposed to radial injection, tests on the axial-injection motor demonstrate its absolutely stable operation. Note that the increasing pressure during the run is a consequence of the oxygen jet dynamics inside the fuel port, which makes regression rate weakly dependent on mass flux and fuel mass flow rate increase over the burn [19]. Hereafter, attention will be paid to address the aspects that have emerged in these cases.

First of all, a coupling between the chamber and the oxygen feed-system dynamics was excluded as a possible cause for the observed worsening of pressure oscillations. In fact, as can be noted from Fig. 8, pressure disturbances travel back from the combustion chamber up to a section downstream of the venturi throat where the pressure transducer is placed (Fig. 1). Pressure upstream of the throat does not show any fluctuations, demonstrating that the venturi is choked and the oxygen mass flow rate is not affected by the chamber pressure. Note that changing the venturi position on the feed line from 1 to 2 in Fig. 1 did not affect the pressure behavior at all.

The pressure oscillations' frequency can be estimated from the amplitude spectrum derived with the Fourier transform technique. The restrictions to 1 kHz of the overall spectra of pressure signals acquired with PTH over the tests previously shown are reported in Fig. 9. All the spectra from the radial-injector tests show broadband peaks at low frequency, that is, below 50 Hz, which is typical of the intrinsic hybrid instability. The very low-frequency components in the spectra of the axial-injector tests are not meaningful, because they do not show any preferred frequencies. In tests 11-R and 4-A, significant peaks can be noted also around 150–200 Hz. Other peaks appear close to 500 Hz and, at higher frequency, around 950 Hz. However, in all of the cases, pressure spectra yield almost similar behaviors in both axial- and radial-injector motors, except for the peaks' amplitude, which is much lower when the axial injector is used.

Central peaks in the neighborhood of 500 Hz correspond to the first longitudinal acoustic mode of the chamber, for which the frequency can be estimated with the well-known relationship (having supposed an acoustically closed–closed chamber)

$$f_{1L} = \frac{c}{2L} = \frac{\sqrt{\gamma (RT)_{\text{av}}}}{2L} \tag{5}$$

in which L is the combustion chamber length (≈ 0.72 m), and c is the average speed of sound in the chamber. The latter can be calculated at the average thermodynamic properties in the combustion chamber [7]; in particular, assuming an average $(RT)_{\text{av}}$ of 6×10^5 m^2/s^2 and $\gamma = 1.25$, an average speed of sound in the chamber equal to 870 m/s and a frequency of 600 Hz are estimated, which is about 20% higher than the value shown by the pressure spectra. This mismatch can be caused by the geometry of the chamber that is composed of three cylindrical tubes (prechamber, fuel grain, and aft chamber) of different internal diameters. In this case, according to Culick [32], the longitudinal acoustic mode has a frequency lower than that calculated for a constant cross section pipe through Eq. (5).

However, a very good agreement with the measured acoustic frequency is achieved when a model for one-dimensional longitudinal waves, obtained starting from the balance equations of mass, momentum, and energy, is employed [33].

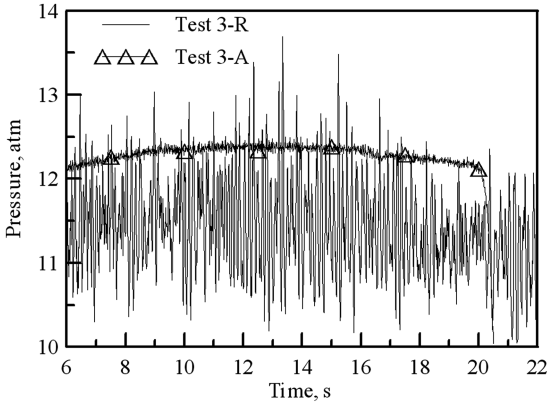

Fig. 7 Chamber pressure versus time, radial injector and axial injector.

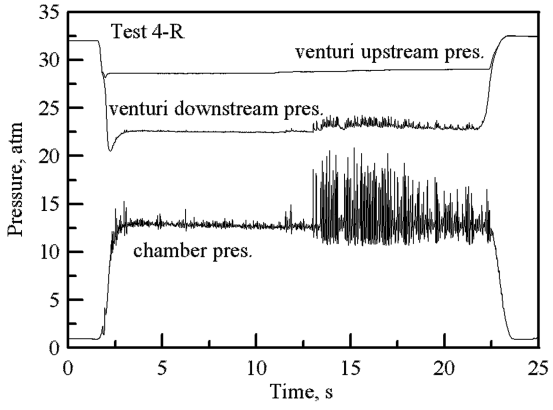

Fig. 8 Pressure upstream and downstream of the venturi throat, and chamber pressure.

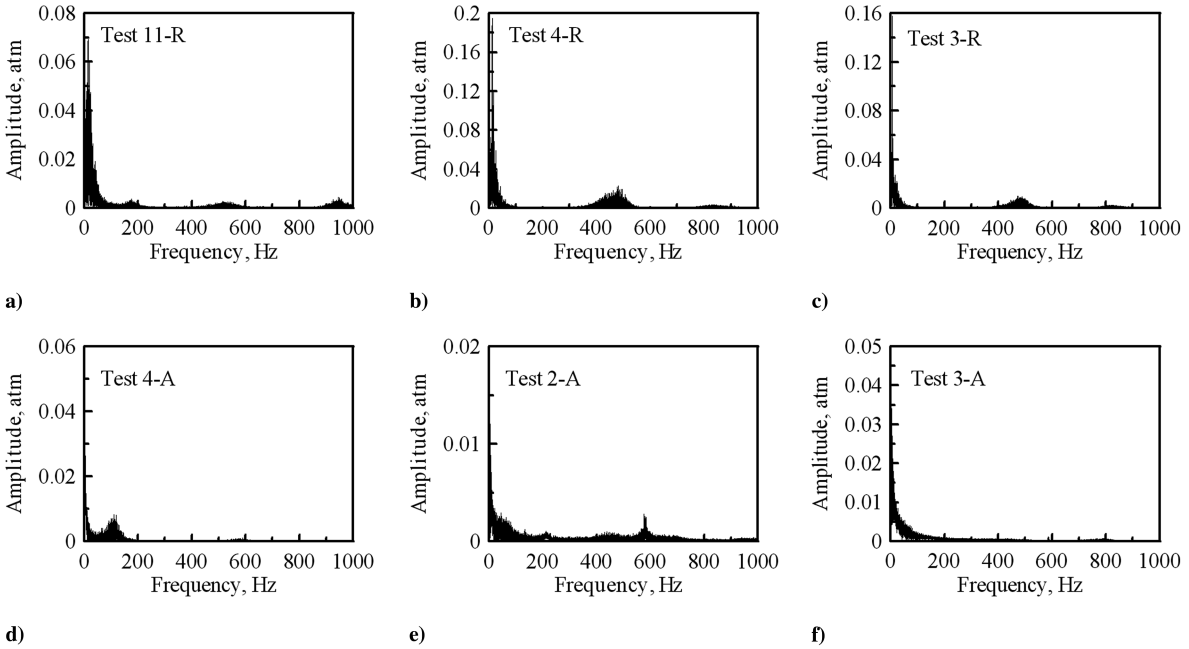

Fig. 9 Pressure amplitude spectra: a–c) radial injector, d–f) axial injector.

The peaks at lower frequency, at about 150 Hz, particularly evident in tests 11-R and 4-A are, instead, due to the Helmholtz mode, whose oscillation frequency is approximately given by [34]

$$f_H = \frac{c}{2\pi}\sqrt{\frac{\pi}{4}\frac{D_t^2}{\mathcal{V}(l+0.8D_t)}} \tag{6}$$

Here, $\mathcal{V}$ is the combustion port total volume, that is, the sum of the prechamber, fuel port, and aft chamber volumes.

This equation predicts, for tests 11-R and 4-A, respectively, a bulk mode frequency that ranges from 29% (at the test startup) to 17% (at the test end), and from 31 to 21% of the longitudinal mode frequency, that is, on the average, around 120–150 Hz, in agreement with the frequency of the secondary peaks shown in Figs. 9a and 9d. Thus, by summarizing, the chamber bulk mode and the first longitudinal acoustic mode appear more or less clearly in all of the tests mentioned, with both the axial and radial injection, whereas the low-frequency instability is typical of the radial-injection motor operation only. Two questions, then, have to be raised: 1) why, in the radial-injector motor, low-frequency instability occurs and acoustic modes are much amplified compared to the axial injector, and 2) why, in certain conditions, the oscillations' amplitude is drastically augmented. The second question will be investigated first.

Low- and high-frequency pressure signals are superimposed for comparison onto the low-frequency regression rate of test 11-R (Fig. 10), over the first and second operating regimes. Note that the regression rate values are definitely higher than could be expected. This is believed to be due to the combination of fuel web compression and thermal effect, which makes the effective speed of sound in the fuel lower than the one in reference conditions. The speed of sound reduction thus induces a higher ultrasound round-trip time (what is actually measured) yielding a nonphysically higher regression rate. Nevertheless, some information may be deduced from the noncorrected regression rate signals.

Figure 10b shows that, during the second regime of intense fluctuations (Fig. 5a), the amplitude of the high-frequency oscillations increases and falls repeatedly in the form of well-defined packets for which the frequency matches the one of the low-frequency pressure fluctuations; the latter frequency is the same as that of the regression rate. Both pressure and regression rate have very similar waveforms of quasi-sinusoidal shape, in particular, fuel regression appears to drive low-frequency pressure oscillations. Hence, a sort of modulation is present between low- and high-frequency signals, which has also been noted in the literature [5,11]. High- and low-frequency oscillation enhancements are also remarkably correlated during the high-fluctuation regime of test 4-R. Moreover, although this modulation appears evident in the second regime, it does not in the low-amplitude oscillation regime (Fig. 10a), in which, although

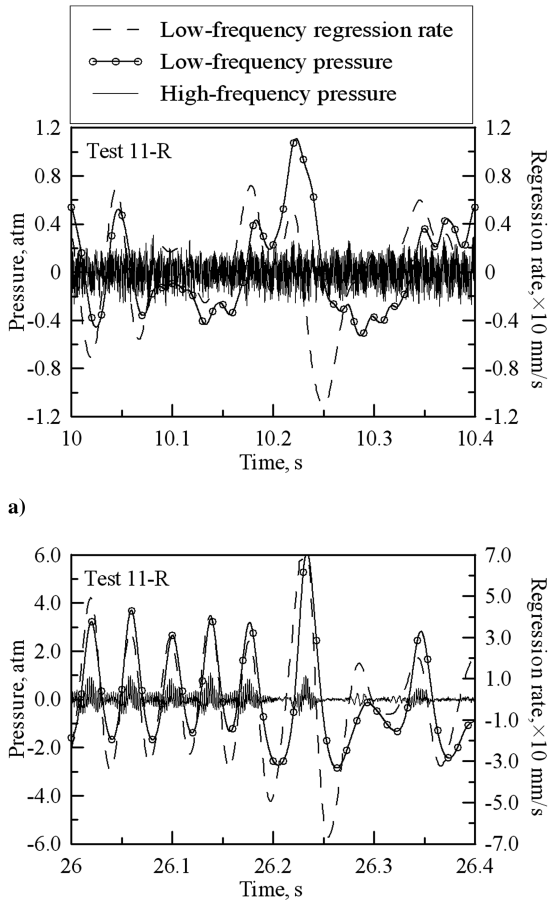

Fig. 10 Time-expanded windows of low- and high-frequency signals, test 11-R: a) first regime, b) second regime.

both low- and high-frequency oscillations are present, they do not seem in phase; additionally, low-frequency pressure and regression rate have different waveforms that do not follow a limit cycle. Test 3-R presents comparable uncorrelation.

This suggests that the simultaneous occurrence of high- and low-frequency oscillations should be the cause for the onset of the highest-amplitude pressure oscillations shown in Figs. 5a and 6.

B. Joint Time-Frequency Domain

An analysis of pressure spectrograms follows to gain more insight into the phenomenon. Figure 11 shows high-frequency pressure spectrograms of tests 11-R and 4-A, each normalized with respect to the corresponding maximum amplitude.

From the pressure spectrogram of the radial-injector motor test (test 11-R, Fig. 11a), it can be noted that the amplitude of the Helmholtz mode is almost constant all over the firing, as demonstrated by the peaks between 150–200 Hz; whereas, only in the early phase of the run, that is, over the first operating regime, the second longitudinal acoustic mode, whose frequency is about 950 Hz, is strongly excited. Its amplitude abruptly increases around 10 s, whereas the first longitudinal acoustic mode, expected around 450–500 Hz, cannot be easily detected. At about 23 s, that is, at the beginning of the second regime, the first longitudinal acoustic mode is then excited, achieving the maximum amplitude in the high-frequency spectrogram.

Test 4-A, in comparison with test 11-R, shows wider band peaks around the first longitudinal acoustic mode, whose frequency shifts from around 400 Hz to around 630 Hz over the burning; the frequency of the second longitudinal mode increases as well. This is evident from the beginning of the test. In this case, the representation of the spectrogram has been restricted to the range $[200, 1200]$ Hz $\times$ $[4, 24]$ s to eliminate the peaks linked to the Helmholtz mode (for which the amplitude is the largest over the test; see also Fig. 9d) and those due to ignition, which would otherwise overshadow the acoustic modes.

This frequency upward shift, shown by the axial-injection tests, is significantly higher than that revealed by the radial-injection firings, most likely because of both the shift in the mixture ratio and the widening of the recirculation region at the entrance of the grain consequent on the port diameter enlargement. The latter causes the bulk temperature in the prechamber to increase for the improved mixing and the higher regression rate, thus resulting in a higher sound speed.

Furthermore, along the very first stage of the run, between 8–11 s, high-frequency oscillations are present around 1120 Hz, which departs from the second longitudinal acoustic mode. Note that a slight increase of the average pressure is yielded during this period (Fig. 5b), as in test 11-R. Around 18 s, the amplitude of the first acoustic mode sharply amplifies.

Therefore, a conclusion is that, regardless of the injection technique, longitudinal acoustic modes exist but they are well damped in the axial-injector motor.

Pressure and regression rate low-frequency spectrograms of test 11-R (Fig. 12) reveal that the peaks of both pressure and regression rate occur approximately at the same frequency with the same relative amplitude. High fluctuations, with a frequency between 15 and 25 Hz, happen in the second regime, when the first longitudinal acoustic mode is triggered. Note that, at the time of maximum activity of this acoustic mode, around 26 s (Fig. 11a), pressure and regression rate oscillation frequency attains the maximum value around 25 Hz. This unveils the nature of coupling between high- and low-frequency fluctuating pressure and regression rate previously observed in Fig. 10. In fact, it is now clear that the second longitudinal acoustic mode of the chamber is triggered first, which manifests itself with a small increase of the average chamber pressure, but the combustion instability intensity remains low; later into the firing, the first longitudinal acoustic mode is amplified and is accompanied by high-amplitude oscillations of the low-frequency pressure and regression rate.

C. Vortex Shedding

The observed order of excitation of the second and first longitudinal modes, respectively, implies that a triggering mechanism has

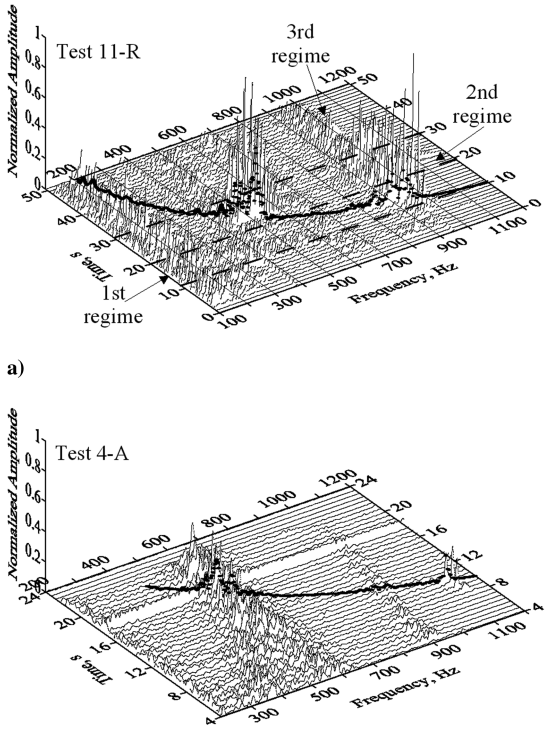

Fig. 11 High-frequency normalized spectrograms of pressure: a) test 11-R, b) test 4-A.

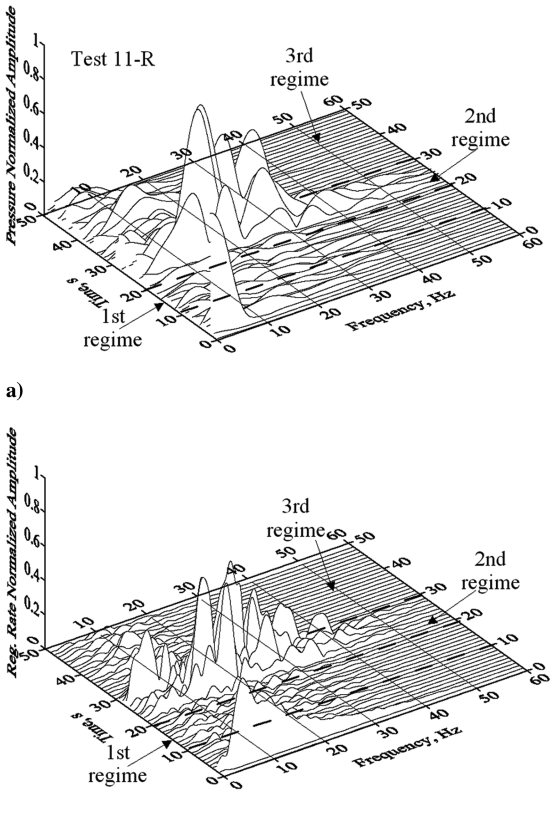

Fig. 12 Low-frequency normalized spectrograms: a) pressure, b) regression rate (test 11-R).

to exist that depends on frequency, such that the latter decreases with the burning time. Actually, combustion instabilities with typical frequency locking-in and decreasing trend with time have often been recognized to be caused by the interaction between vortex shedding, originating from an unstable flow separation in the motor, and chamber acoustics. This phenomenon has been studied especially in solid propellant rockets, but it pertains, in general, to every configuration with an abrupt change in the cross-sectional area of the combustion chamber. Accordingly, vortex shedding from the rearward facing step in the postcombustion chamber was considered as a likely cause for this behavior.

Vortex shedding is a phenomenon of a fluid-dynamic instability nature that occurs in the shear layer present between high- and low-speed streams, for instance, at a sudden expansion. A comprehensive account on the subject is given in [35,36]. Only rarely has vortex shedding been examined as a source of combustion instability in hybrid rockets [16]. Nevertheless, it is believed to play a central role here. Vortices are formed when the instabilities in the shear layer, developing from the edge of the grain at the passage to the aft-mixing chamber (Fig. 13), roll up into coherent structures.

The frequency of this initial roll up mostly depends on the fluid-dynamic characteristics of the velocity profile at the step. However, studies of free and ducted nonreacting jets have established that the preferred mode Strouhal number of the velocity fluctuations at the end of the jet core varies in the range of $0.25 \leq Sr_j \leq 0.5$, where Sr_j is defined as follows

$$Sr_j = \frac{f_j D}{U} \tag{7}$$

In this formula, D and U are, respectively, the jet exit diameter and velocity, and f_j is the preferred mode frequency, which is typically in the second or third subharmonic range of the initial shear layer instability [36]. The shed vortices translate downstream through the chamber at a velocity proportional to, and generally lower than, the one of the mean flow, and significant energy can be transferred into the acoustic field when vortical structures impinge on a solid surface, such as the nozzle entrance, if the point of separation and the point of impingement are located at a suitable distance [12].

At constant Strouhal number, Eq. (7) leads to decreasing shedding frequency as the fuel burns, diameter increases, and gas velocity decreases. Moreover, there are a lot of experimental and numerical results which prove that, if the shedding frequency of vortices equals the frequency of one of the acoustic modes, significant driving of the acoustic oscillation can be generated. Hence, both the observed growth and decay of the oscillations and the time sequence of acoustic modes excitation are consistent with the fact that periodically shed vortices may provide additional acoustic energy. To support this hypothesis, the vortex-shedding frequency was estimated as a function of time and superimposed on the frequency-time plane of the waterfall plots in Fig. 11, where the dotted curves represent the normalized pressure amplitude at the given shedding frequency. The latter was calculated starting from Eq. (7) and introducing the definitions of the theoretical exhaust characteristic velocity and combustion efficiency as follows:

$$c^*_{\text{th}} = \frac{\sqrt{(RT)_{\text{th}}}}{\Psi_{\text{th}}} = \frac{c^*}{\eta} = \frac{\pi}{4}\frac{D_t^2 p}{\eta \dot{m}} = \frac{1}{\eta}\frac{\sqrt{RT}}{\Psi} \tag{8}$$

where

$$\Psi_{\text{th}} = \sqrt{\gamma\left(\frac{2}{\gamma+1}\right)^{\frac{\gamma+1}{\gamma-1}}} \tag{9}$$

and the subscript th refers to the ideal case. Expressing the average velocity at the grain exit as

$$U = \frac{4}{\pi}\frac{\dot{m}}{D^2}\frac{RT}{p} \tag{10}$$

assuming that the function Ψ does not change from the ideal to actual case, and combining Eq. (7) (which is now adjusted to describe the phenomenon at the exit of the grain duct) with Eqs. (8) and (10), the following relationship is yielded:

$$f_{\text{VS-aft}} = \eta c^*_{\text{th}} \Psi^2_{\text{th}} Sr \frac{D_t^2}{D^3} \tag{11}$$

which shows a strong dependence of the vortex-shedding frequency $f_{\text{VS-aft}}$ on the grain diameter and, to a much lower extent, on the mixture ratio, mainly through the characteristic exhaust velocity. This implies that the grain diameter is the main factor influencing the phenomenon. The parameters appearing in the last equation were calculated by means of a ballistic procedure explained in [9]; 0.5 was assigned to the Strouhal number, this being the value associated with a cutoff frequency [12].

From Fig. 11, it can be immediately deduced that, when the shedding frequency of vortices originating at the grain outlet lip approaches the frequency of either the second or the first longitudinal mode, the oscillation amplitude grows with both the radial and axial injector. Based on this idea, one should expect that, in test 4-R (Fig. 6), matching between the vortex-shedding and acoustic frequency has to be verified at approximately 13 s, and, in test 3-R (Fig. 7), it should be totally absent. In fact, Fig. 14 (where normalized pressure spectrograms and chamber pressure are plotted on the same time scales) exactly confirms what was supposed, revealing that, in test 4-R, the vortex-shedding frequency is lower than the second longitudinal mode frequency all over the test, and it approaches the first longitudinal mode one between 10 and 15 s, that is, when the pressure fluctuation is the largest in the firing. Whereas, in test 3-R, the shedding frequency is always smaller than the first acoustic mode one, so that no interactions can take place and the pressure oscillation amplitude remains almost constant.

Coupling between the acoustic field and periodic vortex shedding occurs if the frequencies of both phenomena are nearly equal and if there is a proper impingement point. Indeed, when the shed vortices, consisting initially of unmixed oxygen, vaporized fuel, and hot combustion products, impinge on the nozzle surface, they can burn vigorously due to fine-scale, intense mixing. The impulsive heat release creates a pressure wave; if the latter has the appropriate frequency and phase (which depends on the impingement distance), it can drive acoustic modes, inducing velocity perturbations at the grain edge where separation takes place. Note that the standoff distance from the vortex generation point and the impact surface has to contain at least one vortex [14]. This condition translates into achieving a sufficiently low Mach number in the fuel port, which is usually satisfied in practical situations. The acoustic component of the velocity influences the process of vortex formation, modulating its frequency and completing a feedback loop in the system.

To definitely confirm that coupling between vortex shedding and acoustics is responsible for the steep increase of pressure fluctuations, two tests were carried out, one with a HTPB grain and the other with a HDPE grain, both having 50 mm initial port diameter.

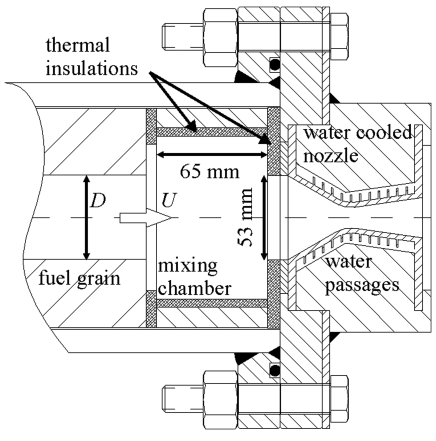

Fig. 13 Motor aft end configuration.

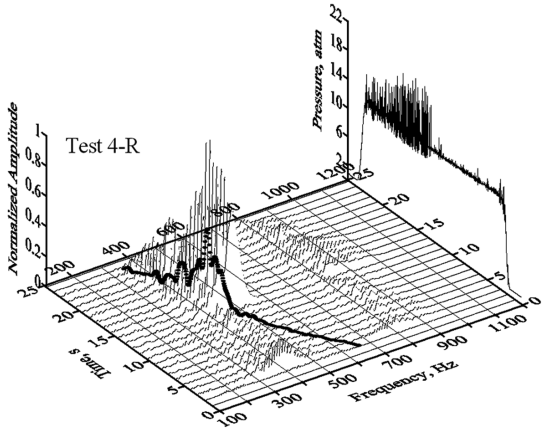

a)

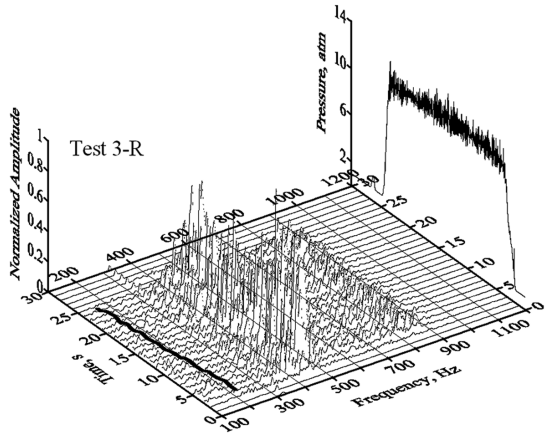

b)

Fig. 14 High-frequency spectrograms and chamber pressure vs time: a) test 4-R, b) test 3-R.

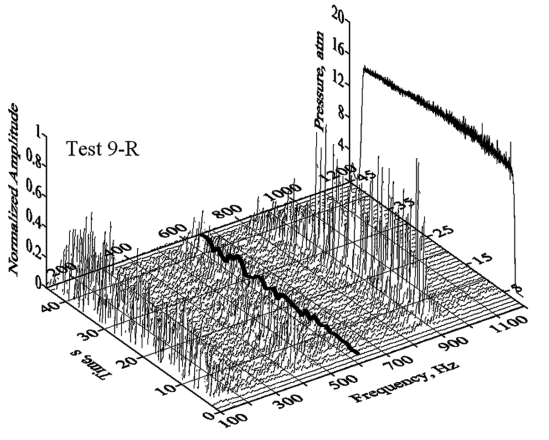

a)

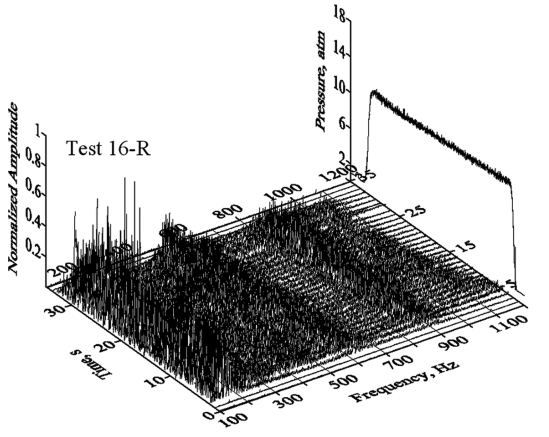

b)

Fig. 15 High-frequency spectrograms and chamber pressure vs time: a) test 9-R, b) test 16-R.

This diameter has been selected to make a comparison with test 4-R. A diaphragm made by thermal insulation was inserted at the end of the grain, between the grain itself and the aft-mixing chamber, in both tests (see Fig. 13). One diaphragm with 50 mm inner diameter was used in test 9-R, while the other, with 25 mm diameter, was used in test 16-R, with the purpose of restricting the vortex-shedding frequency variation in a small range. The diaphragms were not consumed, as was verified after the run. The pressure-time traces and the high-frequency spectrograms of these tests are reported in Fig. 15.

The fundamental aspect is that, in both cases, no combustion instability amplification occurs. In the first case (test 9-R), the estimated vortex-shedding frequency is constantly around 620 Hz, which lies between the first and the second acoustic mode. The second longitudinal mode is the most amplified over the test; this does not seem clear and is probably due to the inaccuracy with which the vortex-shedding frequency is evaluated. In effect, this frequency cannot characterize the phenomenon entirely, because this is indeed much more complex. The vortices, developed in the shear layer inside the mixing chamber, presumably grow and merge as they are convected downstream. Because of merging and entrainment, the shear layer spreads and a sensible change of the characteristic frequency can be yielded. Also in the second case (test 16-R), no instability intensification is shown; the vortex-shedding frequency is definitely out of the acoustic range, around 6 kHz. In fact, no specific acoustic mode is amplified, even though the first and second longitudinal modes are distinguishable along with the chamber bulk mode.

Therefore, the strong pressure oscillations, which develop in tests 11-R and 4-R, are originated by driving the first longitudinal acoustic mode when the frequency of vortex shedding approaches that of the acoustic mode itself. Coupling of vortex shedding with the second acoustic mode does not produce the same destabilizing effects but only a dc shift, most probably because damping at higher frequency is larger [37]. This phenomenon can be seen in test 11-R, but it is particularly noteworthy in test 15-R. Pressure, regression rate, and temperature of the nozzle cooling water are reported as a function of time in Fig. 16; this shows that, by analogy with test 11-R, distinct operating regimes can be clearly defined based on the different chamber pressure behaviors and oscillation magnitudes. The first regime, here, settles between 10 and 17 s, when the second longitudinal mode is driven; the second regime covers the interval 22–32 s, over which the first longitudinal mode is instead amplified. The main difference with test 11-R is that, in this case, the third

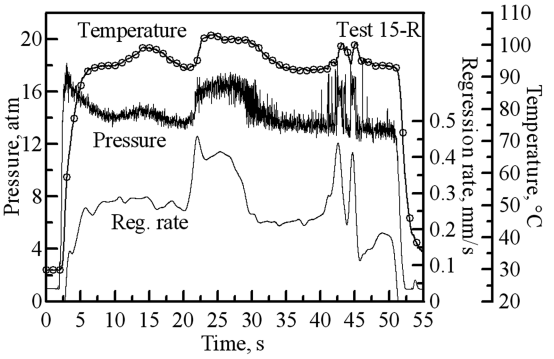

Fig. 16 Pressure, regression rate, and water temperature vs time (test 15-R).

regime, from 40 s to the end of the test, is characterized by the largest oscillation amplitude, which corresponds to a reexcitation of the first longitudinal mode, maybe as a consequence of an increase of the number of vortices along the standoff distance. However, it is noticeable that, as also analyzed in the literature [30], when one of the acoustic modes becomes unstable, the increase of the average pressure is accompanied by a corresponding growth of the average regression rate. Test 15-R has also been chosen for discussion because it allows one to faithfully capture this behavior; indeed, fuel is HDPE, which is stiffer than HTPB [38], so that ultrasonic measurement of regression rate is considerably less influenced by the pressure effect.

The fact that solid-fuel pyrolysis rate is raised in the presence of a resonant acoustic mode is due to the effect of acoustic velocity on both convective heat transfer and mixing [39,40]. Note that the cooling water temperature follows the average pressure trend, demonstrating an effective increase of heat transfer. Coming back to Fig. 10b, it can then be hypothesized that the periodic rise of the regression rate is driven by the augmentation of the heat flux toward the solid-fuel surface when the acoustic mode is triggered by vortex shedding. The fuel vaporized in excess and unreacted is transported downstream and, once it has reached the aft-mixing chamber, it can be efficiently entrained in the vortices, mixed with oxygen, and burned through the vortices' impingement on the nozzle wall. The acoustic mode is thus further driven by the heat released locally by combustion. Low-frequency pressure spikes occur as a consequence of regression rate oscillations, as can be deduced again from Fig. 10b, in which the pressure signal appears to lag the regression rate. It is interesting to observe that, in test 15-R, during the second and third regime, when the high-frequency oscillations are predominantly due to the first longitudinal mode amplification, different behaviors are displayed. In fact, in the second regime, a significant dc shift arises but the pressure fluctuation amplitude remains bounded to around 10% peak to peak; whereas, in the third regime, the average pressure does not shift up remarkably, but large pressure spikes appear with peak-to-peak amplitude around 40%. This may be caused by different amounts of heat released by vortices' combustion. Indeed, the hybrid motor operates over this test with average oxidizer-to-fuel ratio varying with time in the range 4.2–6.2, but, in the third regime, due to the regression rate net increase, from about 0.2 to 0.4 mm/s (Fig. 16), the effective mixture ratio decreases of about 50%, getting close to the stoichiometric value (∼2.7), at which the heat released is expected to be maximum.

D. Low-Frequency Oscillations

Regression rate fluctuations seem to drive low-frequency pressure oscillations in highly unstable operating conditions (Fig. 10b). Remember that, as already discussed in Secs. IV.A and IV.B, low-frequency spectrograms of chamber pressure and regression rate show peaks in the same regions of the time-frequency domain (Fig. 12). By detecting these peaks, it is possible to compare the dominant frequencies as a function of time for a given test. Figure 17 depicts the trends of both the regression rate and pressure frequency for test 11-R.

These trends further highlight what was previously observed from the low-frequency spectrograms and time signals. The regression rate oscillation frequency is, on the average, higher than the pressure frequency; between 25–27 s, when the oscillation amplitude is the largest over the burn, the frequencies exactly overlap. Thus, at least during highly unstable operations, the low-frequency mode is inherently connected with the fuel mass generation fluctuations, which are primarily driven by the heat flux augmentation through acoustic modes, as argued earlier. The same idea is advanced in [5]. This mechanism is also in general agreement with what is stated in [8,41]; in this latter article, based on a linear simplified model derived from the L^* theory for solid propellants, it is shown that combustion oscillations lead pressure oscillations for all the values of the mixture ratio. The dominant frequency of these oscillations is therefore expected to be described by Eq. (1), whose output (calculated by means of the ballistic procedure mentioned before) is plotted in

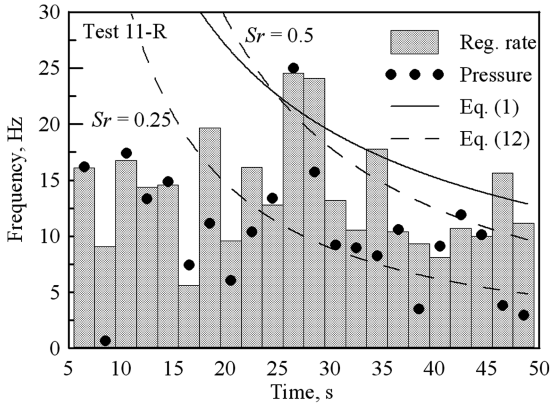

Fig. 17 Pressure and regression rate dominant frequencies vs time; comparison with the hybrid rocket dominant frequency and head-end vortex-shedding frequency (test 11-R).

Fig. 17 for comparison. The measured frequencies appear definitely overestimated by Eq. (1); however, it has to be remarked that the growth of the oscillation frequency, observed during strong instability (25–27 s), shifts the values toward the theoretical curve. A similar comparison is drawn between the results predicted by Eq. (1) (now evaluated at the average parameters in the burn) and the dominant frequencies in the overall spectra of pressure (Table 1) and regression rate. Figure 18 displays the measured dominant frequency versus the predicted frequency; all the data refer to the radial-injector tests because in no cases has a low-frequency instability been observed with the axial injector.

This figure confirms that the observations concerning test 11-R hold true for all the tests: regression rate and pressure have almost the same oscillation frequency, except in some cases where the regression rate frequency is larger; Eq. (1) predicts significantly higher oscillation frequency; the secondary dominant frequency of pressure, determined not as the global spectrum peak frequency but as the local peak frequency during periods of highly unstable operation (whenever these are present) is rather close to the predicted frequency (as demonstrated by the square points in Fig. 18).

This probably means that, only in the radial-injector motor, some phenomena characterized by a frequency lower than the hybrid low-frequency instability, should occur dominating the overall pressure spectrum. Some information to disclose this question can be gathered from two particular tests performed with the radial injector. These tests (test 6-R and test 12-R) were expected to show the same behavior as the other ones, that is, an instability amplification when the acoustic modes and vortex-shedding frequencies were close to each other. Instead, at the same conditions of other radial-injector tests, they displayed a smooth operation (Fig. 19) such as that of the axial-injection motor.

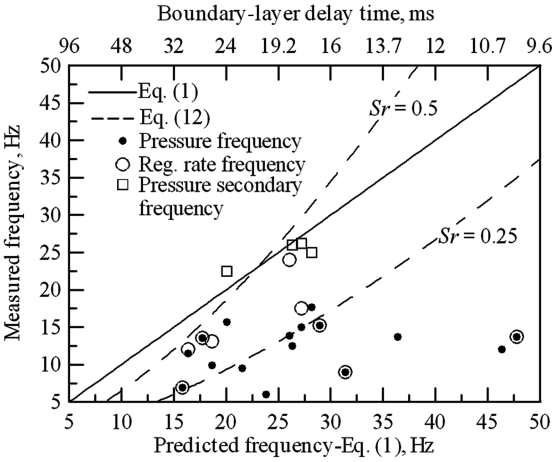

Fig. 18 Comparison between the hybrid rocket dominant frequency, measured frequency, and head-end vortex-shedding frequency.

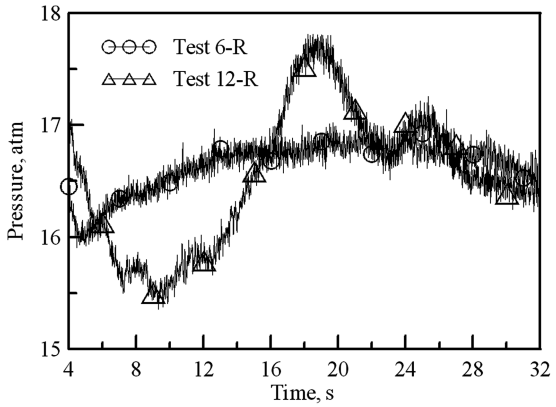

Fig. 19 Chamber pressure vs time: test 6-R and test 12-R.

Both tests were affected by some leakage at the fuel port interface with the prechamber, as was demonstrated by a larger fuel consumption at the port entry and by the characteristic carbon black color of the grain forward face and external surface. The leakage was caused by a wrong mating of the prechamber with the fuel grain for the uneven front surface of the grain itself.

In test 6-R, the vortex-shedding frequency matched the first longitudinal acoustic mode frequency at the firing initial phase, as in test 4-R (Fig. 14a), but no noticeable instability happened. In test 12-R, intersection of the shedding frequency and acoustic modes frequency occurs at around 18 and 26 s with the second and first longitudinal mode, respectively. As a result, pressure trace shows an upward shift due to the heat transfer enhancement exactly as in test 4-A. In both tests, the low-frequency instability does not appear. Then, the main driving source for combustion instability should be linked with the thermo-fluid dynamics in the precombustion chamber. This could be, in general, an unsteady heat release due to the flame holding at the grain entry [5], and/or, maybe also in this case, vortex shedding from the lip of the grain could provide the supposed unsteadiness. Regarding the vortex shedding at the inlet of the grain, a rough estimation of its frequency was performed through Eqs. (7) and (10), using the oxygen mass flow rate and density:

$$f_{\text{VS-pre}} = Sr\frac{4}{\pi}\frac{\dot{m}_{\text{ox}}}{D^3}\frac{R_{\text{ox}}T_{\text{ox}}}{p} \tag{12}$$

This relation implies that, even in this very different configuration compared to the aft chamber, the port diameter is assumed as the characteristic length of the phenomenon, but referring to the flow reattaching distance or the step height (Fig. 3b) might be more realistic; however, this uncertainty can be taken into account through the Strouhal number value. Vortex-shedding frequencies are plotted both in Fig. 17 (ballistically calculated values) and Fig. 18 (values calculated at the average parameters) for the minimum and maximum Sr limits. It is clear that the measured low frequencies are in the range of the shedding frequencies. Therefore, it may be supposed that the shedding of vortices in the passage from the prechamber to the fuel grain could take place, promoting local combustion perturbations. In fact, at the grain inlet, fuel vapor evolving from the grain surface and oxygen are poorly mixed, and the flame is rather likely near the lean limit [5]. In this condition, small perturbations of the mixture ratio will produce very large fluctuations in the local reaction rate and in the energy released in the combustion process [42]. Isolated pressure spikes occurring from the beginning of tests 4-R and 9-R would occur when fuel vapor becomes sufficiently premixed with oxidizer to efficiently ignite the mixture.

Vortices' dynamics could periodically provoke heat release fluctuations of the flame by changing the conditions for local turbulent mixing of the combustible mixture with the hot combustion gases, so that pressure oscillations, with frequency close to the vortex shedding one but lower than the hybrid intrinsic instability, could be the result of this phenomenon. Regression rate would be consequently affected by the influence of the combustion waves on the convective heat transfer. No resonance with the acoustic modes can establish because the frequencies of the involved phenomena are very different. However, the acoustic component of velocity can certainly contribute, on a different time scale, to the mixing process and unsteady heat release in this zone; note that the prechamber

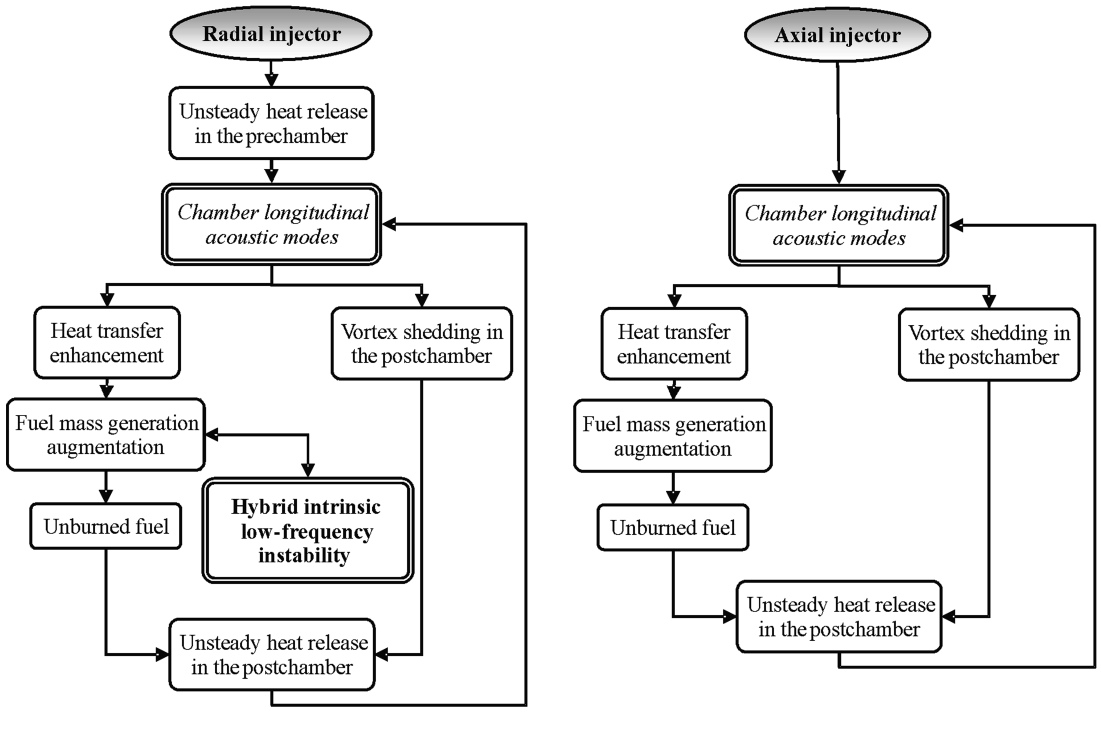

a) b)

Fig. 20 Interaction of acoustics, vortex shedding, and low-frequency instability during a resonant cycle in dependence on the oxidizer-injection technique.

length is exactly one-eighth of the total chamber length and, based on the Rayleigh criterion, this position is preferred for driving both the first and second longitudinal acoustic modes [43].

Hence, the flow pattern generated by the radial injector (Fig. 3a) is responsible, on the one hand, for the low-frequency activity, probably due to the vortex shedding induced perturbations, and, on the other, of the lean flame structure particularly sensitive to acoustics-driven variations. The wide recirculation extending in the port with the axial injection (Fig. 3b) promotes more efficient mixing of reactants ahead of the combustor port, raises the local regression rate and gas temperature, and shifts the mixture ratio far from the lean range, avoiding both flow separation and propellants unmixedness. This hypothesis needs to be verified, of course. However, leakage observed in tests 6-R and 12-R could have changed the velocity profile and the gas temperature at the inlet of the grain, thus changing the local vortex-shedding frequency and/or the flame structure, resulting in conditions more similar to those of the axial injection.

An attempt to elucidate the actual mechanism in the precombustion chamber leading to instability will be made by performing unsteady, reactive numerical simulations as future developments.

V. Conclusions

The focus of this paper was the assessment of the oxidizer-injection effects upon the hybrid rocket combustion stability. Two different configurations were employed which generated, on the one hand, a large recirculation at the motor head end by means of an axial conical nozzle feeding oxygen and, on the other, more uniform flow through a radial injector. The latter, by radially feeding the oxygen in the forward dump plenum, avoids the formation of a jetlike pattern inside the fuel port.

Although most likely a liquid oxidizer will be used in actual motors, and a properly designed injector will be arranged (probably different from purely radial or axial), the purpose of this work was to study basic features of the hybrid engine operation, despite the means by which they are in fact achieved. The firing tests conducted with the axial injector did not show any significant pressure oscillations (i.e., instability); in particular, longitudinal acoustic modes can be noted but they are unconditionally well damped. No low-frequency instability was detected. Whereas the radial injector caused oscillations, the amplitude of which drastically increased when the frequency of the vortex shedding approached the frequency of the first longitudinal acoustic mode. Pressure spectra evidenced the presence of low-frequency activity in the range of 6–18 Hz, which is lower than the typical hybrid-instability frequency. Fuel egression rate oscillates with the same frequency as pressure, and it seems to lead the low-frequency pressure fluctuations in the highly unstable phases, that is, when coupling between acoustics and vortex shedding establishes. In this situation, the frequency of these pressure oscillations increases and shifts toward the intrinsic hybrid instability. Coupling with vortex shedding, actually takes place in the axial-injector hybrid engine as well, but pressure oscillations remain bounded in all conditions. The reason why vortex shedding in the aft chamber does not have the same effect on the motor stability with the two different injectors was attributed to the amplification of the acoustic modes by an additional distinct mechanism. In fact, with the radial injector, unsteady heat release most likely takes place at the entrance of the grain, due to local vortex shedding and/or inadequate flame holding, which is, instead, removed by means of the axial injector. Thus, the primary source of instability lies in the thermo-fluid dynamics in the prechamber.

The complex chain of phenomena is schematically represented in Fig. 20; a flowchart explains what happens in the motor equipped with the two injectors in a resonant cycle, that is, when the fundamental acoustic mode is destabilized by the interaction with the vortex shedding. If the radial injector is used, periodic heat release takes place in the prechamber (due to local vortex shedding, for instance, but not necessarily) and acoustic modes are triggered (Fig. 20a). Pressure oscillations of low amplitude (around 10–15% of the mean pressure) are observed, with acoustic and nonacoustic frequency. The nonacoustic fluctuations have a frequency mostly lower than the hybrid instability dominant frequency and could represent the sign of the unsteady heat release in the prechamber. In this condition, if the frequency of the vortex shedding (in the aft chamber) is close to that of one of the acoustic modes, driving arises. Coupling with the first longitudinal mode strongly raises the oscillation amplitude, which attains its maximum value. In fact, the enhanced periodic heat flux to the fuel surface brings the regression rate up and triggers the low-frequency hybrid instability. The dominant frequency measured over these phases is fairly predicted by the thermal lag-combustion coupled model. Note that acoustic modes are here hypothesized to drive the hybrid low-frequency instability and not vice versa (as supposed to in [11]) because the low-frequency instability occurs only when the first longitudinal mode is driven by the vortex shedding in the postchamber. Otherwise, one should expect that low- and high-frequency instability coexist in other phases of the firing when acoustic modes are unstable. The fuel vaporized in excess burns with unreacted oxygen (note that the radial-injector motor generally operates with oxidizer rich mixture; see Table 1) through the vortex impingement on the nozzle surface, generating sudden heat release and closing a resonant loop.

If the primary cause of acoustic modes excitation, that is, unsteady heat release in the prechamber, is suppressed, with the axial injector (Fig. 20b), for instance, longitudinal acoustic modes are efficiently damped, the heat transfer augmentation is poor, and the hybrid instability is not triggered, so that coupling with the vortex shedding in the aft-mixing chamber has a minor effect.

In conclusion, an effective way of suppressing instability in hybrid rockets seems to develop engine configurations which, first, do not produce unsteady heat release at the motor head end (such as the one induced by vortex shedding), that is, a sufficient condition for instability, and, possibly, result in aft vortex-shedding frequency far from the chamber first longitudinal mode.

Acknowledgments

Part of this work has been funded by Minstero Italiano dell'Istruzione, dell'Università e della Ricerca. The author would like to thank Michele Spiezia for his precious support to the test campaign conduction, and Raffaella Conte for the computational fluid dynamics analyses. I would like to express my special gratitude to Annamaria Russo Sorge who has given me the unique opportunity to research in the field of propulsion. Thanks very much.

References

[1] Culick, F. E. C., and Yang, V., "Prediction of the Stability of Unsteady Motions in Solid Propellant Rocket Motors," *Nonsteady Burning and Combustion Stability of Solid Propellants*, edited by L. De Luca and M. Summerfield, Vol. 143, Progress in Astronautics and Aeronautics, AIAA, Reston, VA, 1992, Chap. 18, pp. 719–779.

[2] Culick, F. E. C., "Combustion Instabilities in Propulsion Systems," *Unsteady Motions in Combustion Chambers for Propulsion Systems*, Research and Technology Organisation AGARDograph, AG-AVT-039, Dec. 2006, Chap. 1.

[3] Roum, R. L., Beckstead, M. W., Finlinson, J. C., and Brooks, K. P., "A Review of Rijke Tubes, Rijke Burners and Related Devices," *Progress in Energy and Combustion Science*, Vol. 19, No. 4, 1993, pp. 313–364. doi:10.1016/0360-1285(93)90007-2

[4] Netzer, D. W., "Hybrid Rocket Internal Ballistics," Chemical Propulsion Information Agency Publ. No. 222, Naval Postgraduate School, Monterey, CA, Jan. 1972.

[5] Boardman, T. A., Brinton, D. H., Carpenter, R. L., and Zoladz, T. F., "An Experimental Investigation of Pressure Oscillations and Their Suppression in Subscale Hybrid Rocket Motors," AIAA Paper 95-2689, July 1995.

[6] De Zilwa, S., Karabeyoglu, M. A., and Zilliac, G., "Combustion Oscillations in High Regression Rate Hybrid Rockets," AIAA Paper 2003-4465, July 2003.

[7] Karabeyoglu, M. A., and Altman, D., "Dynamic Modeling of Hybrid Rocket Combustion," *Journal of Propulsion and Power*, Vol. 15, No. 4, 1999, pp. 562–571. doi:10.2514/2.5464

[8] Karabeyoglu, M. A., De Zilwa, S., Cantwell, B., and Zilliac, G., "Modeling of Hybrid Rocket Low Frequency Instabilities," *Journal of*

Propulsion and Power, Vol. 21, No. 6, 2005, pp. 1107–1116. doi:10.2514/1.7792

[9] Carmicino, C., and Russo Sorge, A., "Influence of a Conical Axial Injector on Hybrid Rocket Performance," *Journal of Propulsion and Power*, Vol. 22, No. 5, 2006, pp. 984–995. doi:10.2514/1.19528

[10] Pucci, J. M., "The Effects of Swirl Injector Design on Hybrid Flame-Holding Combustion Instability," AIAA Paper 2002-3578, July 2002.

[11] Karabeyoglu, A., "Combustion Instability and Transient Behavior in Hybrid Rocket Motors," *Fundamentals of Hybrid Rocket Combustion and Propulsion*, edited by M. J. Chiaverini, and K. K. Kuo, Vol. 218, Progress in Astronautics and Aeronautics, AIAA, Reston, VA, 2007, pp. 351–411.

[12] Flandro, G. A., "Vortex Driving Mechanism in Oscillatory Rocket Flows," *Journal of Propulsion and Power*, Vol. 2, No. 3, 1986, pp. 206–214. doi:10.2514/3.22871

[13] Dotson, K. W., Koshigoe, S., and Pace, K. K., "Vortex Shedding in a Large Solid Rocket Motor Without Inhibitors at the Segmented Interfaces," *Journal of Propulsion and Power*, Vol. 13, No. 2, 1997, pp. 197–206. doi:10.2514/2.5170

[14] Vuillot, F., "Vortex-Shedding Phenomena in Solid Rocket Motors," *Journal of Propulsion and Power*, Vol. 11, No. 4, 1995, pp. 626–639. doi:10.2514/3.23888

[15] Brown, R. S., Dunlap, R., Young, S. W., and Waugh, R. C., "Vortex Shedding as a Source of Acoustic Energy in Segmented Solid Rockets," *Journal of Spacecraft and Rockets*, Vol. 18, No. 4, 1981, pp. 312–319. doi:10.2514/3.57822

[16] Greiner, B., and Frederick, R. A., Jr., "Experimental Investigation of Labscale Hybrid Instability," AIAA Paper 94-2878, June 1994.

[17] Cauty, F., "Solid-Propellant Combustion Response Function from Direct Measurement Methods: ONERA Experience," *Journal of Propulsion and Power*, Vol. 15, No. 6, 1999, pp. 837–843. doi:10.2514/2.5503

[18] Murphy, J. J., and Krier, H., "Evaluation of Ultrasound Technique for Solid-Propellant Burning-Rate Response Measurements," *Journal of Propulsion and Power*, Vol. 18, No. 3, 2002, pp. 641–651. doi:10.2514/2.5978

[19] Carmicino, C., and Russo Sorge, A., "Role of Injection in Hybrid Rockets Regression Rate Behavior," *Journal of Propulsion and Power*, Vol. 21, No. 4, 2005, pp. 606–612. doi:10.2514/1.9945

[20] Carmicino, C., and Russo Sorge, A., "The Effects of Oxidizer Injector Design on Hybrid Rockets Combustion Stability," AIAA Paper 2006-4677, July 2006.

[21] Carmicino, C., and Russo Sorge, A., "Performance Comparison Between Two Different Injector Configurations in a Hybrid Rocket," *Aerospace Science and Technology*, Vol. 11, No. 1, 2007, pp. 61–67. doi:10.1016/j.ast.2006.08.009

[22] Jacovitti, G., and Scarano, G., "Discrete Time Technique for Time Delay Estimation," *IEEE Transactions on Signal Processing*, Vol. 41, No. 2, 1993, pp. 525–533. doi:10.1109/78.193195

[23] Eriksson, H., Börjesson, P. O., Ödling, P., and Holmer, N. G., "A Robust Correlation Receiver for Distance Estimation," *IEEE Transactions on Ultrasonics, Ferroelectrics, and Frequency Control*, Vol. 41, No. 5, 1994, pp. 596–603. doi:10.1109/58.308494

[24] Wear, K. A., "The Effects of Frequency-Dependent Attenuation and Dispersion on Sound Speed Measurements: Applications in Human Trabecular Bone," *IEEE Transactions on Ultrasonics, Ferroelectrics, and Frequency Control*, Vol. 47, No. 1, 2000, pp. 265–273. doi:10.1109/58.818770

[25] Traineau, J. C., and Kuentzmann, P., "Ultrasonic Measurements of Solid Propellant Burning Rates in Nozzleless Rocket Motors," *Journal of Propulsion and Power*, Vol. 2, No. 3, 1986, pp. 215–222. doi:10.2514/3.22872

[26] Carmicino, C., "Alcuni Aspetti della Balistica Interna di un Endoreattore a Propellenti Ibridi e del Comportamento di Ugelli a Spina Troncata," Ph.D. Dissertation, Univ. of Naples "Federico II", Naples, Italy, Nov. 2002.

[27] Dénos, R., and Olivari, D., "Digital Data Acquisition and Processing," *Measurement Techniques in Fluid Dynamics: An Introduction*, 2nd ed. revised, von Karman Inst. for Fluid Dynamics, Rhode-St-Genèse, Belgium, 2001.

[28] Mertins, A., *Signal Analysis: Wavelets, Filter Banks, Time-Frequency Transforms and Applications*, Wiley, New York, 1999, pp. 196–202.

[29] Malhotra, S., and Flandro, G. A., "On Nonlinear Combustion Instability," AIAA Paper 97-3250, July 1997.

[30] Karabeyoglu, A., "Thermal Transients in Hybrid Rocket Fuel Grains: Nonlinear Effects," AIAA Paper 2007-5369, July 2007.

[31] Story, G., Zoladz, T., Arves, J., Kearney, D., Abel, T., and Park, O., "Hybrid Propulsion Demonstration Program 250 K Hybrid Motor," AIAA Paper 2003-5198, July 2003.

[32] Culick, F. E. C., "Some Fundamentals of Acoustics," *Unsteady Motions in Combustion Chambers for Propulsion Systems*, Research and Technology Organisation AGARDograph, AG-AVT-039, Dec. 2006, Chap. 5, pp. 21–23.

[33] Pastrone, D., Casalino, L., Sentinella, M. R., and Carmicino, C., "Acoustic Analysis of Hybrid Rocket Combustion Chambers," AIAA Paper 2007-5368, July 2007.

[34] De Zilwa, S., Zilliac, G., Reinath, M., and Karabeyoglu, M. A., "Time-Resolved Fuel-Grain Port Diameter Measurement in Hybrid Rockets," *Journal of Propulsion and Power*, Vol. 20, No. 4, 2004, pp. 684–689. doi:10.2514/1.2188

[35] Shadow, K. C., and Gutmark, E., "Combustion Instability Related to Vortex Shedding in Dump Combustors and Their Passive Control," *Progress in Energy and Combustion Science*, Vol. 18, No. 2, 1992, pp. 117–132. doi:10.1016/0360-1285(92)90020-2

[36] Kailasanath, K., and Gutmark, E. J., "Combustion Instability," *Propulsion Combustion: Fuels to Emissions*, edited by G. Roy, Taylor and Francis, Washington, D.C., 1998, pp. 129–172.

[37] Matveev, K. I., and Culick, F. E. C., "A Model for Combustion Instability Involving Vortex Shedding," *Combustion Science and Technology*, Vol. 175, No. 6, 2003, pp. 1059–1083. doi:10.1080/00102200302349

[38] Cauty, F., Carmicino, C., and Russo Sorge, A., "The Pressure Sensitivity of the Ultrasonic Waves Velocity: A Contribution to a Better Determination of the Energetic Material Regression Rate," *Proceedings of the 6th International Symposium on Special Topics in Chemical Propulsion, Advancements in Energetic Materials and Chemical Propulsion*, K. Kuo, and J. de Dios Rivera (eds.), Begell House, Redding, CT, Jan. 2007, ISBN 978-1-56700-239-3.

[39] Matta, L. M., Zinn, B. T., and Jagoda, J. I., "Experimental Study of Acoustic Velocity Effects on Simulated Solid Fuel Pyrolysis," *AIAA Journal*, Vol. 35, No. 9, 1997, pp. 1493–1498. doi:10.2514/2.273

[40] Matta, L. M., Zhu, C., Jagoda, J. I., and Zinn, B. T., "Mixing by Resonant Acoustic Driving in a Closed Chamber," *Journal of Propulsion and Power*, Vol. 12, No. 2, 1996, pp. 366–370. doi:10.2514/3.24037

[41] Jenkins, R. M., and Cook, J. R., "A Preliminary Analysis of Low Frequency Pressure Oscillations in Hybrid Rocket Motors," AIAA Paper 95-2690, July 1995.

[42] Lieuwen, T., Neumeier, Y., and Zinn, B. T., "The Role of Unmixedness and Chemical Kinetics in Driving Combustion Instabilities in Lean Premixed Combustors," *Combustion Science and Technology*, Vol. 135, 1998, pp. 193–211. doi:10.1080/00102209808924157

[43] Matveev, K., "Thermoacoustic Instabilities in the Rijke Tube: Experiments and Modeling," Ph.D. Dissertation, California Inst. of Technology, Pasadena, CA, 2003.

T. Lieuwen
Associate Editor